Birefringence-induced frequency beating in high-finesse cavities by continuous-wave cavity ring-down spectroscopy

Patrick Dupré*

Laboratoire de Physico-Chimie de l' Atmosphère, Université du Littoral, Côte d'Opale, 189A Avenue Maurice Schumann, 59140 Dunkerque, France

(Received 11 August 2015; published 6 November 2015)

By analyzing the decaying intensity, leaking out a high-finesse cavity previously "filled" by a cw laser source (using the cavity ring-down spectroscopy technique), we observed frequency beating between what we think are two orthogonal eigenpolarization states of the intracavity electromagnetic field. The time decay (ring down) is analyzed by varying the angle of the polarization analyzer located in front of the detector. A full modeling of the observed signal is proposed. It is based on the Jones matrix formalism required for modeling the cavity behavior following a rotated phase shifter. The full transfer function is first established in the frequency domain, and then Fourier transformed to recover the temporal response. The same optical cavity, i.e., constituted of the same set of mirrors, is used at two different wavelengths (∼800 and ∼880 nm). It demonstrates the differences in behavior between a high-finesse cavity (∼400 000) and a lower finesse cavity (∼50 000). Beating frequency, characteristics time, and beat amplitude are mainly discussed versus the analyzer angle. A cavity birefringence of $\sim 1.6 \times 10^{-5}$ rad, resulting from the mirror birefringence is suggested. If the current analysis is in agreement with pulsed CRDS experiments (polarimetry) obtained in an isotropic moderate-finesse cavity, it differs from a recent work report on a high-finesse cavity associated with a source mode locking [Phys. Rev. A **85**, 013837 (2012)].

DOI: 10.1103/PhysRevA.92.053817 PACS number(s): 42.60.Da, 42.25.Ja, 42.25.Lc, 42.79.Bh

I. INTRODUCTION

Birefringence in optical cavities has been the subject of numerous publications in recent decades. Pioneering work can probably be ascribed to Le Floch and Le Naour [1] who first observed the doubling of the cavity modes in a low-finesse (∼50) cavity by inducing polarization anisotropy using intracavity waveplates.

Studies of spatial anisotropies have a much longer history which cannot be facilely summarized; however, they are strongly related to modern science, including physics, chemistry, and biology. Anisotropic media are valuable environments for testing the fundamental properties of the physical interactions. Despite the absence of a complete review, we will only mention a limited list of hot topics here: parity nonconservation (PNC) [2], magnetic vacuum birefringence (BMV), molecular chirality [3], Kerr and Cotton-Mouton effects in gases [4], optical anisotropy, and tests of predictions of the quantum electrodynamics (QED) [5]. It is worth noting that when using an electromagnetic field (EMF), the extension of its interaction length has been seen as a possible means to improve the detectivity of minuscule effects. Hence, first, multipass cells, and later, optical cavities have been promoted as crucial devices. The accumulation of the number of round trips is expected to "amplify" the anisotropy effects as it does for standard linear absorption. Nevertheless, the intrinsic birefringence attached to interferential mirrors can be seen as an inconvenience because the residual birefringence background can potentially mask much weaker but desirable signals.

Because high-finesse optical cavities seem to be optimum devices to quantify the anisotropy effects, it is of crucial interest to well characterize the relevant behavior. Actually, the dielectric (interferential) multilayer coatings deposited on the substrate are key components since they experience the multiple round trips of the intracavity EMF. It has been observed early on that the coating stacks, comprising the reflectors, exhibit residual intrinsic birefringence [6] (for a review see Ref. [7]), which is barely controlled by the manufacturers. On the contrary, the mirror substrates are crossed only one time by the EMF, and they weakly contribute to the total anisotropy.

Residual birefringence in high-finesse cavities has already drawn significant attention since the availability of high reflectors leading to cavities with finesse approaching 10^6 [8,9], thanks to the continuous improvements in the coating technology. Such a high value of the finesse remains exceptional; however, optical cavities are now finding applications in numerous domains. We can identify spectral narrowing of laser [10], detection of weakly absorbing species, generation of intense EMFs, gravity wave detection, gas and vacuum birefringence exploration, high resolution spectroscopy, polarimetry, surface science, and frequency metrology. The unique properties of high-finesse cavities result from an EMF interference pattern arisen between, at least two high reflectors, and basically controlled by the cavity length. A high control of the cavity alignment, and of the injection of the EMF, allow featuring frequency combs, structured by the cavity free-spectral range (FSR). In addition, the linear response of the cavity or/and medium (i.e., assuming the proportionality of the intracavity losses with the intensity of the impinging EMF [11]) is usually easy to model while the nonlinear behaviors can require considerable consideration. Furthermore, the use of a "multichromatic" EMF can be a source of additional complexity [12].

Broadband or incoherent sources may fail to match the basic behavior discussed here. Nonetheless, if the frequency extension of the source is less than the cavity FSR, the overall high-finesse cavity behavior can be simplified to a single resonant cavity mode (TEM_{00}) matching a strict

*pdupre@gmx.com

Lorentzian shape. Such a spectral response provides all the properties of interest. For example, the temporal response to an impulsional (or substitutable) excitation is a pure exponential decay. Accordingly, any distortion of such behavior requires careful attention. For instance, nonlinear response of the intracavity medium, such as saturated absorption, is one of these "nonstandard" behaviors [13].

This paper is devoted to the analysis of linear birefringence in a cavity. Actually, several experimental techniques, EMF polarization based, can be implemented to study such an effect. Probably the most customary one is the measurement of an extinction ratio observable between a polarizer, and a rotary and possibly adjustable analyzer. This is conceptually an extension of the prior birefringence and dichroism technique, applied to multipass cavities [6,14], and to resonant cavities [7,15–23]. CW resonant cavities require frequency locking of the cavity against the source, or vice versa, of the source against the cavity. Another technique consists of measuring directly the birefringence induced by the cavity mode frequency separation [24,25]. Actually, considering a very high-finesse cavity, such measurements can be very accurate when measuring the beating frequency between two injected beams if each of them is locked on the relevant eigenpolarization cavity mode. The last technique, which can be mentioned, is based on the temporal analysis of the cavity response as it can be implemented in cavity ring-down spectroscopy (CRDS). Theoretically, similar information can be extracted from time or from frequency measurements. This technique has been pioneerly implemented by the Vaccaro group by using a pulsed source and moderate-finesse cavities. It has been implemented to measure the linear birefringence and circular dichroism of chiral species (measurement of a differential beating frequency) [26–28]. Later, it has been extended to polarimetry and ellipsometry of surfaces at Forth [29–33]. The latter group has also set up nonlinear-shaped cavities (rectangle or butterfly geometry) to approach chirality in pulsed mode [34], and PNC in continuous mode [35,36]. When the birefringence is weak, the frequency beating may not be observable during the decay time, and only changes of ring-down (RD) times versus the analyzer angle can be reported even for a high-finesse cavity [37,38].

The cavity birefringence reported in this paper is based on the now well established CRDS technique (for reviews see Refs. [39–47], and its prior developments [48,49]) in continuous-wave (cw) mode. All the information about the cavity and the surrounded medium can be deduced from the temporal response. CRDS has gained its popularity because of its conceptual simplicity and high sensitivity when high-finesse cavities are set up.

In the vast majority of setups, exponential temporal decays are reported. However, deviations from this typical behavior are numerous. We can distinguish: (i) simple or complex modulations due to the cavity mode beating, sometimes observable when the spectral extension of the source exceeds the cavity FSR [50,51] (typically in pulsed regimes) and if the detection chain (detector, transimpedance amplifier, converter and acquisition device) is fast enough, (ii) bi- or multiexponential decays when the cavity losses are not homogeneous within the spectral extension of the source (such as the case of transition exhibiting a Doppler broadening less than the spectral extension of the pulsed source) [52,53], (iii) time dependent absorption on the time scale of the decay (chemistry), and (iv) nonlinear response of the intracavity losses against the intensity of the impinging source (such as the case of saturated absorption in optically thin media [13,54,55]).

In this paper we report essentially on the nonexponential response time of an empty high-finesse cavity at two different wavelengths (i.e., around 795 and 880 nm) by using a unique set of mirrors and a high resolution cw laser source. The very different coefficient of the high reflectors at these two wavelengths provides noticeable different RD times (almost one order of magnitude) under standard conditions. By installing a rotary polarization analyzer in front of the CRDS detector, we acquired, what we think, to the best of our knowledge, is the first observation of frequency beating (amplitude controllable) induced by the residual high-finesse cavity birefringence (cavity under vacuum). Indeed, the cavity birefringence lifts the degeneracy of two orthogonal polarization cavity eigenstates.

The full cavity time response is established by using the Jones matrix formalism and by identifying the optical cavity to a rotated phase retarder, characterized by ϵ (i.e., the effective cavity birefringence), the resulting dephasing between the s and p polarizations, and θ, the azimuthal rotation of the effective dephasor. By varying the polarization analyzer angle, beating frequency (relevant for the highest finesse cavity only), RD time, and modulation amplitude are carefully discussed with regards to the experimental data.

The reported analysis is in good agreement with induced birefringence inside a moderate-finesse cavity obtained by using a pulsed source [26,34], but it is not in agreement with a recent analysis obtained with a high-finesse cavity devoted to the detection of the magnetic vacuum birefringence [23]. This mismatch is discussed.

The effective cavity birefringence (ϵ) is measured with an accuracy of $\sim 10^{-7}$ rad which is certainly poor in comparison with what is required for highly demanding measurements. However, no real effort has been made to calibrate the cavity length. Furthermore, the fluctuations around the mean value of ϵ still needs to be understood before making further progress.

II. EXPERIMENTAL SETUP

The experimental setup implemented the usual CW-CRDS technique complemented by a polarization analyzer (see Fig. 1). The laser chain was based on a scanable, externally stabilized Ti:sapphire laser source (Coherent model 899-21) capable of delivering up to 2 W in single longitudinal mode (frequency stability: $\sim$1 MHz rms) when it is optically pumped by an Ar^+ laser source (Spectra Physics, model 2045). By using a beam splitter (BS, actually uncoated BK7 plates set at 45° in p polarization) a small fraction ($\sim$1% per interface, the useless reflection was blocked) of the outgoing laser beam was directed to a homemade interferometric lambdameter [56] for selecting the wavelength of interest. In this paper we report about two different wavelengths (796 and 879 nm) which were kept constant during the data acquisitions.

The high-finesse CRDS cavity was built around a homemade chamber (aggregating pieces of aluminum and of stainless steel) supporting two high reflectance ($\mathcal{R} \sim 0.9999925$ at

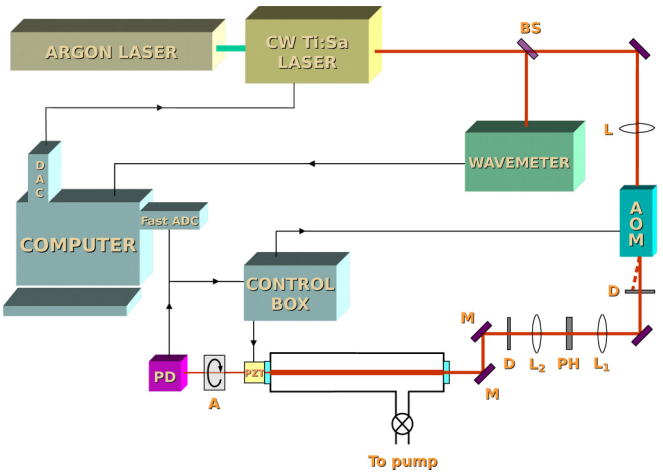

FIG. 1. (Color online) Experimental setup. Cavity length ∼0.35 m, radius of curvature (ROC) of the mirrors ∼1 m. Abbreviations are as following: PD is a photodiode, PH is a pinhole, AOM is an acousto-optics modulator, BS is a beam splitter, D are circular apertures, M are periscope mirrors, PZT is a piezoelectric actuator, L_1 and L_2 are two focusing lens, and A is a polarization analyzer.

796 nm) superpolished planoconcave mirrors ∼0.35 m apart (ROC ∼ 1 m, diameter ∼7.75 mm, thickness ∼4 mm) from Research Electro Optics (run 0X524). The "output" mirror sat on an annular cylindrical piezoelectric (PZT) actuator (Physik Instruments) allowing the control of the cavity length. The incoming beam was "cleaned" by a spatial filter (association of the lens L_1, the pinhole PH, the lens L_2, and the aperture D). The spatial power distribution of the cropped central lobe of the diffracted beam is very close to the Gaussian profile of a pure TEM_{00} transverse mode. The adjustable position of the lens L_2 complemented by the periscope (mirrors M_1 and M_2) provided a good match between the laser beam and one of the TEM_{00} modes of the evacuated cavity: a rejection rate of the non-TEM_{00} modes of 1:100 or less was routinely obtained. The beam transmitted through the cavity was collected on a silicon detector (Hamamatsu, model S3399; diameter: 1.5 mm) feeding a homemade large bandwidth transimpedance amplifier (feedback resistor: $R_F = 30\ \mathrm{k}\Omega$) associated with an additional fast amplifier (gain 10). This photodetector, preceded by a polarization analyzer, was used for both cavity control and RD time acquisition.

A homemade control box allowed tracking a narrow cavity mode (∼2 kHz, FWHM at 796 nm) of the high-finesse cavity ($\mathcal{F} \sim 420\,000$, only ∼50 000 at 879 nm) compared with the "large" time-averaged laser spectral width (∼1 MHz). There was no tight locking of the laser source against the optical cavity; however, a mode tracking was obtained by feeding back the high voltage on the PZT actuator. It allowed the cavity length to be slightly dithered to provide maximum transmission of the cavity.

Therefore, with more detail: the control box generated a low frequency (50–500 Hz) amplitude modulated high-voltage, superimposed to a dc voltage (maintaining a positive value to the resulting voltage), and directed to the PZT actuator through a current driver. It provided a cavity length modulation whose peak-to-peak amplitude matched several times the cavity bandwidth (i.e., at resonance). When tracking was operated (i.e., after the automatic detection of a cavity mode), the correction signal tuned the dc component of the voltage to balance the modulated voltage against the cavity transmission [47]. Thus, the maximal power trapped inside the cavity was determined by initially trimming a voltage threshold which triggered the acquisition chain. The intracavity power build-up time was actually determined by the value of this threshold, the modulation amplitude, the impinging power, the cavity finesse, and the percentage of collected beam (i.e., depending on the polarization analyzer angle, see Sec. IV). The effective intracavity power value was well below the theoretical maximum power: $\mathcal{I}_0\mathcal{F}/\pi$ ($\mathcal{I}_0$ is the impinging power) only reachable when the source is tightly locked against the cavity [57,58].

In addition, the trigger signal was used, (i) to interrupt the cavity length modulation in preparation to the data acquisition, (ii) to "switch off" the laser beam through a current driven acousto-optics modulator (AOM from AA Opto-Electronique), and (iii) to trigger (with a delay) the data acquisition chain. The AOM was activated by a rf current at 80 MHz (2 W) building up an acoustic grating diffracting the impinging red beam in the order −1 (the diffraction order zero was dumped). The switching time was estimated to less than 100 ns. The rf power rejection rate (between the off and on transmission modes) was higher than 70 dB; it is obtained by a Mini-Circuits switch device.

The entire setup was driven by a personal computer (PC), the graphic-user-interface application (virtual instrument) was implemented by using Labview (National Instruments). The application allowed the acquisition of the RD decay by a 12-bit analog-to-digital converter (ADC) sampling up to 5 MHz (National Instruments acquisition card). Several RD decays could be summed up (actually up to several thousands) before or/and after the data transfers. The full acquisition time (t_{aq}) could differ for each data acquisition (see Sec. IV B).

The cavity was evacuated by dual root blowers (250 + 500 m^3/h).

For the present analysis, no wavelength scan of the Ti:sapphire laser was required. The two wavelength values considered were simply provided by reading the wavemeter through an asynchronous serial line.

The Ti:sapphire laser provided a linearly polarized beam whose direction remained unchanged (i.e., vertical [s polarization]) at the input of the optical cavity. A manually adjustable, high rejection rate polarizer, sat in front of the photodetector. The optimization of the cavity finesse was obtained by maximizing the RD time in absence of polarization analyzer.

III. CRDS SIGNAL MODELING

A Cartesian system of coordinates will be assumed: z is the propagation direction, x is the direction of the s polarization, and y is the direction of the p polarization.

Considering the EMF impinging on the photodetector and ignoring its transverse dependence (cylindrical beam), we can depict its amplitude in the slowly varying envelop

approximation (SVEA) [59] by

$$\boldsymbol{E}_{\rm det}(\omega,z) = 2\pi\ \boldsymbol{E}_{\rm out}(\omega) \otimes\left[\boldsymbol{\delta}(\omega-\omega_0)\,e^{-ikz} + \boldsymbol{\delta}(\omega+\omega_0)\,e^{ikz}\right], \quad (1)$$

where $k=\omega/c$ is the usual wave vector, ω is the angular pulsation (usually also called frequency in this work) spanning the frequency space (time conjugated), c is the speed of the light in vacuum, and ω_0 is the carrier frequency. $\boldsymbol{E}_{\rm out}(\omega)$ is the Fourier transform of the amplitude of a time dependent real signal (see Appendix in Ref. [12], it defines the frequency extension of the detected signal), $\otimes$ represents the convolution product, and $\boldsymbol{\delta}(\omega)$ is the usual Dirac function [60].

Actually, the EMF $\boldsymbol{E}_{\rm out}(\omega)$ is a vector (here a Jones vector) with components $\boldsymbol{E}_{\underset{y}{\rm out}x}(\omega)$ along the directions x and y [the same property applies to $\boldsymbol{E}_{\rm det}(\omega,z)$]. $\boldsymbol{E}_{\rm out}(\omega)$ can be obtained from the EMF impinging on the optical cavity $\boldsymbol{E}_{\rm imp}(\omega)$ by applying the Jones matrix well established transformations [61]. For an empty cavity, in absence of birefringence information about the individual mirrors constituting of the optical cavity, we will assume that the coating of the couple of high reflectors can be depicted by an oriented linear retarder (i.e., a rotating differential phase shifter) with the Jones matrix

$$M_0(\theta,\epsilon) = \begin{bmatrix} \cos\frac{\epsilon}{2} + i\,\cos(2\theta)\,\sin\frac{\epsilon}{2} & i\,\sin(2\theta)\,\sin\frac{\epsilon}{2} \\ i\,\sin(2\theta)\,\sin\frac{\epsilon}{2} & \cos\frac{\epsilon}{2} - i\,\cos(2\theta)\,\sin\frac{\epsilon}{2} \end{bmatrix}, \quad (2)$$

where θ is the azimuth of the fast axis of the linear retarder, and where ϵ is the shifting phase angle [62]. It is worth noting that the matrix $M_0(\theta,\epsilon)$ is unitary but not Hermitian.

The full Jones matrix linking $\boldsymbol{E}_{\rm out}(\omega)$ to the EMF impinging $\boldsymbol{E}_{\rm imp}(\omega)$ can be obtained by ignoring the pure propagation (no absorption), except inside the cavity (where interference arise), and by considering each identified optical elements.

A. Eigenpolarizations

Assuming that both identical mirrors ($L_{\rm cav}$ apart) can be represented by diagonal matrices for the transmission and the reflection, and do not exhibit additional losses, it becomes

$$\boldsymbol{E}_{\rm out}(\omega) = M_{\rm Pol}(\alpha) \times \boldsymbol{M}_{\rm cav}(\omega;\,\theta,\epsilon) \times \boldsymbol{E}_{\rm imp}(\omega), \quad (3)$$

where $M_{\rm Pol}(\alpha)$ is the Jones matrix of the polarizer, set at the azimuthal angle α [62], and where $\boldsymbol{M}_{\rm cav}(\omega;\,\theta,\epsilon)$ is given by

$$\boldsymbol{M}_{\rm cav}(\omega;\,\theta,\epsilon) = \mathcal{T}\sum_{n=0}^{\infty}[\mathcal{R}\,e^{-i\delta}\,M_0(\theta,\epsilon)]^n. \quad (4)$$

$\mathcal{R}$ and $\mathcal{T}$ are the intensity coefficients of the mirrors for the reflection and the transmission, respectively, and where $\delta = 2\pi\omega/\omega_{\rm FSR}$ with

$$\omega_{\rm FSR} = \frac{\pi\,c}{L_{\rm cav}} = \frac{2\pi}{t_{rt}} = 2\pi\,\nu_{\rm FSR}, \quad (5)$$

where t_{rt} is the cavity round-trip time.

The expression of the matrix $\boldsymbol{M}_{\rm cav}(\omega;\,\theta,\epsilon)$ can be easily obtained by diagonalization, i.e., by calculating the polarization eigenvalues and eigenvectors. After calculation of the series expansion, it becomes ($\mathcal{R} \lesssim 1$)

$$\boldsymbol{M}_{\rm cav}(\omega;\,\theta,\epsilon) = M_\lambda^{-1} \times \mathcal{T}\begin{bmatrix} \left(1-\mathcal{R}\lambda_+ e^{-i\delta}\right)^{-1} & 0 \\ 0 & \left(1-\mathcal{R}\lambda_- e^{-i\delta}\right)^{-1} \end{bmatrix} \times M_\lambda, \quad (6)$$

where

$$M_\lambda = \frac{1}{\Delta}\begin{bmatrix} \rho' & \rho\,\sin\beta - \sin\frac{\epsilon}{2} \\ \sin\frac{\epsilon}{2} - \rho\,\sin\beta & \rho' \end{bmatrix} = \begin{bmatrix} \lambda_x^+ & \lambda_x^- \\ \lambda_y^+ & \lambda_y^- \end{bmatrix}, \quad (7)$$

with

$$\Delta = \sqrt{2\left[1-\rho\,\cos\left(\frac{\epsilon}{2}+\beta\right)\right]}, \quad (8)$$

$$\rho' = \sin(2\theta)\,\sin\frac{\epsilon}{2}, \quad (9)$$

$$\rho = \sqrt{\cos^2\frac{\epsilon}{2} + \cos^2(2\theta)\,\sin^2\frac{\epsilon}{2}}, \quad (10)$$

and

$$\tan\beta = \cos(2\theta)\,\tan\frac{\epsilon}{2}. \quad (11)$$

The two polarization eigenvalues are readily obtained:

$$\lambda_\pm = \rho\,\cos\beta \pm i\sqrt{1-\rho^2\,\cos^2\beta} = \cos\frac{\epsilon}{2} \pm i\,\sin\frac{\epsilon}{2} = e^{\pm i\frac{\epsilon}{2}}. \quad (12)$$

It is worth noting that $\lambda_\pm$ are independent of θ (as well of ω). In addition, we have the inequality $\beta \leqslant \frac{\epsilon}{2}$, and the property

$$\rho^2 + \rho'^2 = 1, \quad (13)$$

while the matricial product $M_\lambda^{-1} \times M_\lambda$ is equal to the identity matrix.

B. Behavior close to resonance

The only possibly frequency resonant terms due to the intracavity interference, i.e., providing a non-null response are the two diagonal matrix elements of Eq. (6):

$$\frac{\mathcal{T}}{1-\mathcal{R}\lambda_\pm e^{-i\delta}}. \quad (14)$$

The resonance condition is reached only if $|\mathcal{R}\lambda_\pm e^{-i\delta}| \lesssim 1$, i.e., if $\delta \sim p\pi$ (p is an integer). Hence, following Kastler [48], Hils and Hall [63], and Uehara and Ueda [64], we can define the equivalent filter (or transfer) function for a high-finesse

cavity by

$$\boldsymbol{F}_{\pm}(\omega) = \frac{\mathcal{T}}{1-\mathcal{R}} \sum_{p=0}^{\infty} (-1)^p \left(\frac{1}{1 + \mathrm{i}\dfrac{\omega - p\omega_{\mathrm{FSR}} - \omega_{\mathrm{off}_{\pm}}}{\Delta_\omega}} + \frac{1}{1 + \mathrm{i}\dfrac{\omega + p\omega_{\mathrm{FSR}} + \omega_{\mathrm{off}_{\pm}}}{\Delta_\omega}} \right), \tag{15}$$

where Δ_ω if the half-width at half-maximum (HWHM) of the resonant Lorentzian shape provided by the finesse of the cavity defined by

$$\Delta_\omega = \frac{\omega_{\mathrm{FSR}}}{2\mathcal{F}} = \frac{1-\mathcal{R}}{2\pi\mathcal{R}}\omega_{\mathrm{FSR}} \sim \frac{1-\mathcal{R}}{2\pi}\omega_{\mathrm{FSR}}, \tag{16}$$

and where

$$\omega_{\mathrm{off}_{\pm}} = \frac{\omega_{\mathrm{FSR}}}{2}\left(1 \pm \frac{\epsilon}{2\pi}\right) = \omega_{\mathrm{off}} \pm \frac{\epsilon}{2}\frac{\omega_{\mathrm{FSR}}}{2\pi}. \tag{17}$$

The extension to the negative frequencies has been set to satisfy the fact that $\boldsymbol{F}_{\pm}(\omega)$ are the Fourier transforms of real functions, i.e., $\boldsymbol{F}^*_{\pm}(\omega) = \boldsymbol{F}_{\pm}(-\omega)$.

Hence we can recognize that a frequency comb $\boldsymbol{F}_{\pm}(\omega)$ is associated with each polarization eigenvalues $\lambda_{\pm}$. The two (dual) frequency combs are frequency shifted by $\epsilon\frac{\omega_{\mathrm{FSR}}}{2\pi}$. Obviously, if the finesse of the cavity is too low ($\mathcal{F} < \frac{4\pi}{\epsilon}$), the two combs are quasidegenerated (the offset of the comb, ω_{off} is without importance here and it can be ignored).

The limited extension (Δ_0) of the laser source $\boldsymbol{E}_{\mathrm{imp}}(\omega)$, at least when it is compared with the cavity FSR, allows us to consider only the frequency range around a dual tooth (or resonant mode). The tracking feedback (see Sec. II) allows a good match of the frequency of the laser source with one dual cavity mode. Hence, Eq. (15) can be replaced by

$$\frac{\mathcal{T}}{1-\mathcal{R}}\boldsymbol{f}_{\pm}(\omega) = \frac{\mathcal{T}}{1-\mathcal{R}}\frac{2\pi}{1 + i\frac{\omega}{\Delta_\omega}} \otimes \left[\boldsymbol{\delta}(\omega - \omega_{c_{\pm}}) + \boldsymbol{\delta}(\omega + \omega_{c_{\pm}})\right], \tag{18}$$

with $\omega_{c_{\pm}} = \omega_c \pm \frac{\epsilon}{2}\frac{\omega_{\mathrm{FSR}}}{2\pi}$, and where ω_c is the central frequency of the selected cavity mode.

Finally, by plugging Eq. (18) into Eq. (3), and after calculation of the matrix products, one obtains

$$\boldsymbol{E}_{\mathrm{out}}(\omega) = \frac{\mathcal{T}}{1-\mathcal{R}} M_{\mathrm{Pol}}(\alpha) \times \boldsymbol{M}_{\mathrm{bir}}(\omega;\theta) \times \boldsymbol{E}_{\mathrm{imp}}(\omega), \tag{19}$$

where

$$\boldsymbol{M}_{\mathrm{bir}}(\omega;\theta) = \begin{bmatrix} \Lambda_{xy}\,\boldsymbol{f}_+(\omega) - \Lambda_{yx}\,\boldsymbol{f}_-(\omega) & \Lambda_{\mathrm{dia}}\,[\boldsymbol{f}_+(\omega) - \boldsymbol{f}_-(\omega)] \\ \Lambda_{\mathrm{dia}}\,[\boldsymbol{f}_+(\omega) - \boldsymbol{f}_-(\omega)] & -\Lambda_{yx}\,\boldsymbol{f}_+(\omega) + \Lambda_{xy}\,\boldsymbol{f}_-(\omega) \end{bmatrix}, \tag{20}$$

and where we have defined three new quantities depending only on θ and ϵ :

$$\Lambda_{xy} = \lambda_x^+\lambda_y^- = \frac{\rho'^2}{\Delta^2}, \tag{21}$$

$$\Lambda_{yx} = \lambda_y^+\lambda_x^- = -\frac{1}{\Delta^2}\left(\sin\frac{\epsilon}{2} - \rho\sin\beta\right)^2 = \Lambda_{xy} - 1, \tag{22}$$

$$\Lambda_{\mathrm{dia}} = -\lambda_x^+\lambda_y^+ = \lambda_x^-\lambda_y^- = \frac{\rho'}{\Delta^2}\left(\rho\sin\beta - \sin\frac{\epsilon}{2}\right) = -\sqrt{-\Lambda_{xy}\Lambda_{yx}}. \tag{23}$$

C. Response to a linear polarization

Assuming a vertically polarized impinging EMF [$\boldsymbol{E}_{\mathrm{imp}_x}(\omega) = |\boldsymbol{E}_{\mathrm{imp}}(\omega)|$, $\boldsymbol{E}_{\mathrm{imp}_y}(\omega) = 0$], both Cartesian components of the detected signal can be obtained by using Eq. (19). It becomes

$$\underset{y}{\boldsymbol{E}_{\mathrm{out}x}}(\omega) = \frac{\mathcal{T}}{1-\mathcal{R}}\left[\underset{y}{\xi_{+x}}(\alpha)\,\boldsymbol{f}_+(\omega) + \underset{y}{\xi_{-x}}(\alpha)\,\boldsymbol{f}_-(\omega)\right] \times |\boldsymbol{E}_{\mathrm{imp}}(\omega)|, \tag{24}$$

with

$$\xi_{+_x}(\alpha) = \cos^2\alpha\,\Lambda_{xy} + \sin\alpha\,\cos\alpha\,\Lambda_{\mathrm{dia}}, \tag{25}$$

$$\xi_{-_x}(\alpha) = -(\cos^2\alpha\,\Lambda_{yx} + \sin\alpha\cos\alpha\,\Lambda_{\mathrm{dia}}), \tag{26}$$

$$\xi_{+_y}(\alpha) = \sin^2\alpha\,\Lambda_{\mathrm{dia}} + \sin\alpha\,\cos\alpha\,\Lambda_{xy}, \tag{27}$$

$$\xi_{-_y}(\alpha) = -(\sin^2\alpha\,\Lambda_{\mathrm{dia}} + \sin\alpha\cos\alpha\,\Lambda_{yx}). \tag{28}$$

By setting the polarization analyzer at the angle α, the collected power results from the sum of the intensity of the two components E_{out_x} and E_{out_y}, i.e.,

$$\boldsymbol{I}_\alpha(\omega) = \frac{c\,\epsilon_0}{2}\left[\boldsymbol{E}_{\mathrm{out}_x}(\omega) \otimes \boldsymbol{E}^*_{\mathrm{out}_x}(-\omega) + \boldsymbol{E}_{\mathrm{out}_y}(\omega) \otimes \boldsymbol{E}^*_{\mathrm{out}_y}(-\omega)\right] = \boldsymbol{I}_{\alpha_x}(\omega) + \boldsymbol{I}_{\alpha_y}(\omega). \tag{29}$$

Under the current experimental conditions, we can assume that $\Delta_0 \gg \Delta_\omega$ and that $\Delta_0 \ll \omega_{\mathrm{FSR}}$. Accordingly, we can set (ignoring the propagation factors)

$$\boldsymbol{E}_{\mathrm{imp}}(\omega) = \frac{E_0}{2\Delta_0}\frac{2\pi}{1 + i\frac{\omega}{\Delta_0}} \otimes \left[\boldsymbol{\delta}(\omega - \omega_0) + \boldsymbol{\delta}(\omega + \omega_0)\right], \tag{30}$$

where E_0 is the amplitude of the exponentially time decaying (emulating the temporal coherence) characterizing the impinging EMF.

Under the same conditions, by plugging Eq. (30) into Eq. (24), the product of the two Lorentzian profiles converges toward the narrowest profile. Hence, by using Eq. (29), after ignoring the high frequency interference around $2\omega_0$ while keeping only the low frequency terms, and by assuming the

tuning condition $\omega_0 \simeq \omega_c$, it becomes

$$\boldsymbol{I}_{\substack{\alpha x \\ y}}(\omega) \simeq I_0 \frac{2\pi}{i\omega + 2\Delta_\omega} \otimes \left\{ \left(\xi^2_{\substack{+x \\ y}}(\alpha) + \xi^2_{\substack{-x \\ y}}(\alpha) \right) \delta(\omega) + \xi_{\substack{+x \\ y}}(\alpha)\xi_{\substack{-x \\ y}}(\alpha) \left[\delta\left(\omega - \frac{\omega_{\rm FSR}}{2\pi}\epsilon\right) + \delta\left(\omega + \frac{\omega_{\rm FSR}}{2\pi}\epsilon\right) \right] \right\}, \tag{31}$$

with as usual (ϵ_0 is the vacuum permittivity [or (di)electric constant])

$$I_0 = \frac{c\,\epsilon_0}{2} E_0^2. \tag{32}$$

Finally, by taking the inverse Fourier transform to obtain the temporal behavior and summing the two EMF components, one obtains

$$I_\alpha(t) = I_0\, e^{-t/\tau} \left\{ \xi^2_{+_x}(\alpha) + \xi^2_{-_x}(\alpha) + \xi^2_{+_y}(\alpha) + \xi^2_{-_y}(\alpha) + 2[\xi_{+_x}(\alpha)\xi_{-_x}(\alpha) + \xi_{+_y}(\alpha)\xi_{-_y}(\alpha)] \cos\left(\frac{\omega_{\rm FSR}}{2\pi}\epsilon t\right) \right\} u(t), \tag{33}$$

with $\tau = (2\Delta_\omega)^{-1}$ which is the usual ring-down time (or characteristic time [65]) of the cavity, and where $u(t)$ is the Heaviside step function.

D. Discussion

It is convenient to recast the temporal behavior [Eq. (33)] to emphasize the frequency beating at $f_{\rm mod} = \epsilon \frac{f_{\rm FSR}}{2\pi} = \frac{\epsilon}{2\pi\, t_{rt}}$; indeed, this frequency is independent of the cavity finesse, at least if the two eigencavity modes remain within the cavity bandwidth. This beating is actually superimposed to the usual exponential ring-down decay. The modulation amplitude $m(\alpha)$ is controlled by the analyzer angle α according to

$$I_\alpha(t) = \mathscr{A}(\alpha,\theta)\, e^{-t/\tau} \left[1 + m(\alpha,\theta) \cos\left(\frac{\omega_{\rm FSR}}{2\pi}\epsilon t\right) \right], \tag{34}$$

with

$$\mathscr{A}(\alpha,\theta) = I_0 \left[\xi^2_{+_x}(\alpha) + \xi^2_{-_x}(\alpha) + \xi^2_{+_y}(\alpha) + \xi^2_{-_y}(\alpha) \right], \tag{35}$$

and with

$$m(\alpha,\theta) = \frac{2[\xi_{+_x}(\alpha)\xi_{-_x}(\alpha) + \xi_{+_y}(\alpha)\xi_{-_y}(\alpha)]}{\xi^2_{+_x}(\alpha) + \xi^2_{-_x}(\alpha) + \xi^2_{+_y}(\alpha) + \xi^2_{-_y}(\alpha)}. \tag{36}$$

It is worth pointing out that both quantities, $\mathscr{A}(\alpha,\theta)$ and $m(\alpha,\theta)$, are independent of ϵ. If the phase shift is weak ($\epsilon \ll 1$, and $\epsilon \ll \theta$), it can also be shown that

$$\begin{aligned} &\xi^2_{+_x}(\alpha) + \xi^2_{-_x}(\alpha) + \xi^2_{+_y}(\alpha) + \xi^2_{-_y}(\alpha) \\ &\quad = \tfrac{1}{2}\{1 + \cos(2\theta)\, \cos[2(\theta+\alpha)]\} \end{aligned} \tag{37}$$

and

$$2[\xi_{+_x}(\alpha)\xi_{-_x}(\alpha) + \xi_{+_y}(\alpha)\xi_{-_y}(\alpha)] = \tfrac{1}{2}\sin(2\theta)\, \sin[2(\theta+\alpha)]. \tag{38}$$

Both quantities, $\mathscr{A}(\alpha,\theta)$ and $m(\alpha,\theta)$, have a periodicity of π versus α.

The amplitude of the decay $\mathscr{A}(\alpha,\theta)$ depends strongly on the angle α. This amplitude can reach very small values (even zero) according to the value of θ. This later case is addressed when the analyzer angle is oriented perpendicularly to the impinging polarization ($\alpha \sim \pm\pi/2$) and when θ is small. On the other hand, the amplitude of the decay is maximum when the analyzer angle is parallel to the impinging polarization (*vide infra*).

The coefficient controlling the amplitude of the beating $m(\alpha,\theta)$ varies from -1 to 1 according to the value of α. Singularities (associated with the absence of beating) are predicted around $\pi/2$ and $3\pi/2$ (depending on θ), while around $p\pi$ (p is an integer) the beat amplitude smoothly crosses zero. These singularities can be abrupt if θ approach zero.

IV. DATA ANALYSIS

The analysis of the experimental data has been made possible by using two fit algorithms based on nonlinear least-squares (NLS) minimization (Marquardt-Levenberg procedure): the gnuplot package [66], and the Minuit2 package [67,68] for double checking purposes. If both procedures converge toward the same fitted values without difficulty, the extraction of the standard deviations (STD) on the fitted values requires some attention: although the STDs do not depend on the data weighting in gnuplot, they depend on the data weighting in Minuit2. Anyway, as it is specified in the gnuplot manual the error estimates are over-optimistic quantities and "they should not be used for determining confidence levels, but are useful for qualitative purposes." Overall, we adapted the plotted errors as well as the provided uncertainties by keeping the reduced chi-square factor ($\chi^2_{\rm red}$) [69] close to 1 as recommended. Specific indications are available in the figure captions.

The same set of cavity mirrors has been used for the two wavelengths reported here, i.e., 796 nm (Sec. IV B) and 879 nm (Sec. IV C) (the maximum of reflectance of this set of mirrors is centered around 800 nm). The cavity finesse and the RD decays reported are very different versus the two reported wavelengths. The values of the intracavity power have been determined after evaluating the mirror transmission and the responsivity of the photodetector. We only report data obtained when the cavity is empty, i.e., evacuated.

A. Decays without setting the polarization analyzer

The temporal decays have been first analyzed in the absence of the polarization analyzer to provide reference RD times (τ_0), see Fig. 2. The decays have been fitted by an offset pure exponential function by assuming a constant technical noise (1–2 mV for a unique decay) since the intensity of the collected signal (a few tens of μW at the beginning of the decay) provides a negligible photon-shot noise in comparison with the intrinsic electronics noise, at least for the analyzed decays. The residual noise (difference between the fitted and experimental data) shows an almost uniform noise till ~1.65 ms at 796 nm.

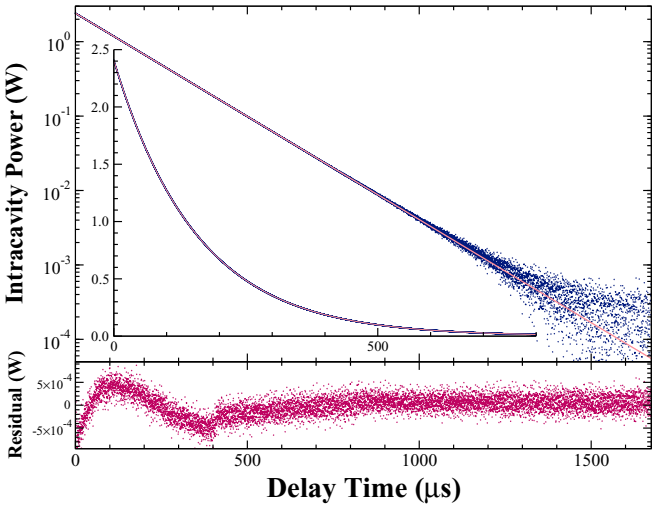

FIG. 2. (Color online) Ring-down decay at 796 nm without an analyzer. 3700 decays have been averaged (total acquisition time $t_{aq} \sim$ 377 s). Log and linear y scales are provided. $\tau_0 = 156.648\,(2)\,\mu$s (exponential decay) has been obtained ($\chi^2_{red} \sim 1$ for $\Delta_y \sim 2.5 \times 10^{-4}$ W). The experimental data are shown in dark blue (dark gray) and the result of the fit are shown in pink (medium gray).

No significant deviation from a pure exponential shape is observable over more than four orders of magnitude (straight line in a logarithmic scale), despite weak unclear residual glitches. The analog-to-digital converter (ADC) has been made up from prior identified conversion nonlinearities, but the corrections may still not be sufficient.

At 879 nm, similar behaviors have been obtained; however, the reference RD time τ_0 is only 18.6379 (9) μs while a less number of samples (acquisition rate: 5 Msamples/s) per decay have been acquired.

B. Behavior of the high-finesse cavity

We present in Fig. 3 the RD decays for a set of analyzer angles (the angle zero has been set approximately to the vertical

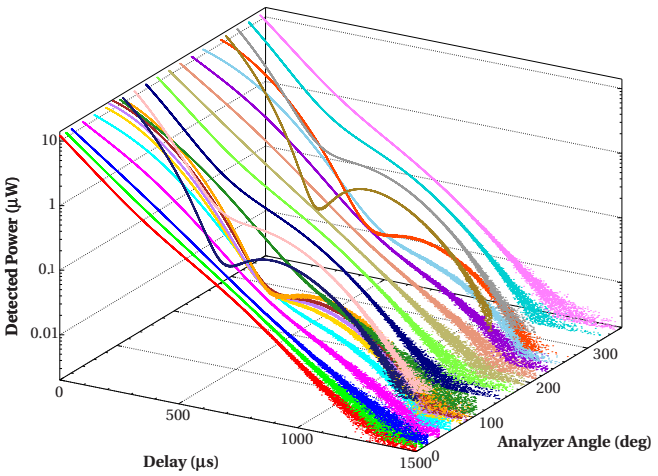

FIG. 3. (Color online) Ring-down decays at 796 nm versus the analyzer angle. The number of averaged decays for each value of α is not constant: it varies from 300 to 3760 (see text).

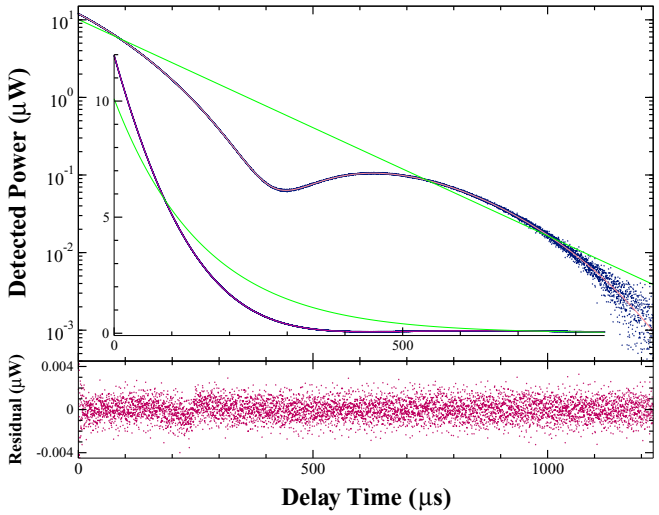

FIG. 4. (Color online) Ring-down decay with beating at 796 nm. The analyzer angle is set at 110°. 2180 decays have been averaged. The experimental data are in dark blue (dark gray) and the result of the fit by a modulated function in pink (medium gray) [$\tau = 155.80\,(2)\,\mu$s, $m = 0.8499\,(1)$, $T = 919.62\,(11)\,\mu$s] (linear and log y scales are shown) The y offset has been subtracted. In green (light gray) the fitted decay without modulation is shown. The given uncertainties have been provided by the fit procedure ($\chi^2_{red} \sim 1$ for $\Delta y \sim 0.001\,\mu$W, see text).

polarization impinging on the cavity, *vide infra*) obtained at 796 nm. An inaccuracy on the analyzer angle of 2.5° has been estimated.

It clearly appears that around 90° and 270° (i.e., when the detected polarization is almost perpendicular to the impinging polarization) the RD decays exhibit a nonexponential shape (indeed, a frequency beating) emphasized by the use of a logarithmic y scale. A detailed view of this behavior obtained at 110° is shown in Fig. 4. It appears that these RD decays can be readily fitted by a frequency modulated decay, i.e., following the formula

$$y(t) = A\left[1 + m\,\cos\left(\frac{2\pi t}{T_{\rm mod}} + \phi\right)\right]\exp\left(-\frac{t}{\tau}\right) + \text{Offset}, \tag{39}$$

where τ is the RD time, m is the modulation index (see Sec. III D), $T_{\rm mod}$ is the period of the modulation, and ϕ is the dephasing of the modulation. This experimental behavior follows perfectly that predicted for a rotated phase shifter [see Eq. (34) where the dephasing (ϕ) has not been considered].

The behavior depicted by Eq. (39) has been used to fit all the decays available at 796 nm (actually two sets of data were recorded on two different days), see Fig. 3. The result of the fitting process for $\alpha = 110°$ is shown in Fig. 4 (setting a uniform weighting). To emphasize the beating, Fig. 4 shows also the result of the fit with a pure exponential decay [in green (light gray)] assuming a RD time $\tau_0 = 156.648\,\mu$s. For this angle set on the analyzer (110°), as well for an angle of 290°, strong modulation indexes $m \sim 0.85$ and $m \sim 0.914$ have been obtained, respectively.

Figure 3 requires special attention when considering the absolute amplitude of the detected signal. The decay acquisition is triggered by a voltage threshold which is the same for all the analyzer positions. This threshold provides an identical initial amplitude for all the decays. Indeed, when the polarizer is close to the crossed polarization angle, the intensity of the transmitted beam is strongly reduced when it is compared with the impinging beam intensity. However, the way that the CRDS detection behaves, induces a longer buildup time to reach a same detection threshold initializing the decay acquisition. It results that a total intensity of the intracavity EMF ($\mathcal{I}_c$) has been increased in the same proportion. The net result was a longer acquisition time (t_{aq}), or/and alternatively, a reduced number of decays averaged. This behavior is perfectly well identified because the acquisition time, for each value of the analyzer angle, has been backed up in the acquisition files. This allows establishing the expected correlations between $\mathcal{I}_c$ and t_{aq}. It follows that we cannot validate experimentally Eqs. (35) and (37). Furthermore, this acquisition mode provides a dephasing of the amplitude modulation (ϕ) which is assumed meaningless.

Although, if we cannot investigate the absolute amplitude of the RD signal, we can still analyze the amplitude of the modulation versus the analyzer angle, it means that relations (36) and (38) can be interrogated. Figure 5 shows the fitted modulation indexes versus the analyzer angle as well the results of the fit processes for two sets of data. It clearly shows the π periodicity and the singularities around 105° and 285° where the modulation index jumps from almost 1 to -1. However, around the abrupt changes of $m(\alpha)$, the data are much more difficult to acquire because of the weak intensity available in p polarization. At the opposite, around $\pi/2$ and $3\pi/2$ (i.e., ∼15° and ∼195°), the modulation index is close to zero, and the decays are easy to characterize.

It is noteworthy that the sign of the modulation index is correlated with the dephasing of the cosine function [see Eq. (39)]. Thus, in case of possible ambiguities, i.e., when the modulation index is weak, a smooth and continuous behavior has been assumed to determine properly the modulation index sign. The fit of the modulation indexes has been performed by using Eq. (36) where an offset (α_{off}) has been set to take into account the shift displayed by the rotating plate driving the polarization analyzer, and accounting for any residual single-pass birefringence. The data weighting has been determined by considering the standard deviations provided by the previous fit steps. Hence, the parameter θ is easily obtained: its small value explains the weak beam intensities detected around $\pi/2$ and $3\pi/2$ as shown by the simulation (see Fig. 6).

Supplementary to the modulation index, two other quantities can be extracted independently from the RD decays: the RD time and the modulation period. The RD times are plotted in Fig. 7(a) while the beating periods are plotted in Fig. 7(b). Although both quantities fluctuate with α, weighted mean values have been derived, 156.7 (6) and 912.8 (3.8) μs, respectively. The relevant discussion including that relative to the error bars, is postponed to Sec. V.

To gain confidence in the present analysis, another set of data has been analyzed [see Fig. 5(b)]. These data have been

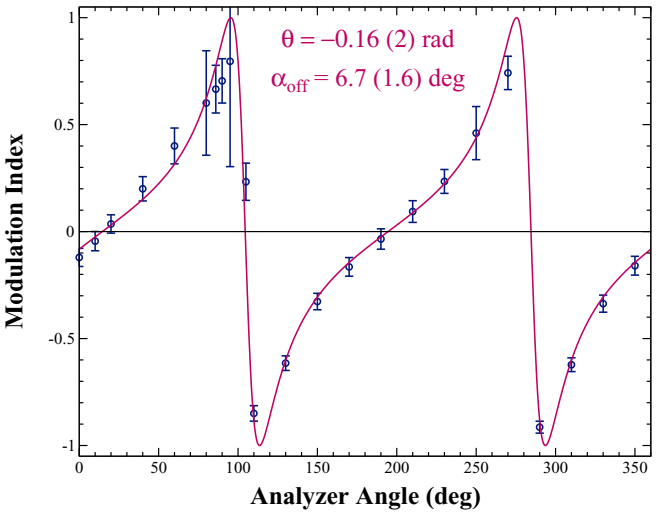

(a)

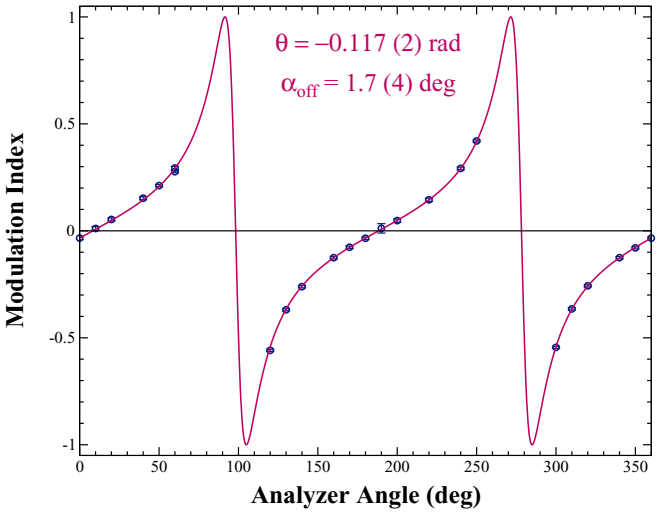

(b)

FIG. 5. (Color online) Modulation index for two sets of data. The experimental data are shown in dark blue (dark gray) and the fitted data in red. (a) Set 1, the error bars are equal to 450 times the STD provided by the fit process of the decays, they provide $\chi^2_{red} \sim 1$. (b) Set 2, the error bars are equal to 30 times the STD provided by the fit process of the decays, they provide $\chi^2_{red} \sim 1$.

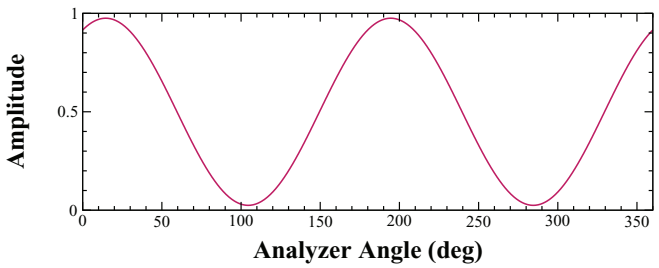

FIG. 6. (Color online) Simulation of the amplitude of the ring-down signal. This simulation has been obtained with the fitted parameters of Fig. 5(a). This modulation would be observed if the intensity of the impinging beam had been kept constant (see text). It is worth noting that the peak-to-peak amplitude is slightly less than 1 (∼0.95).

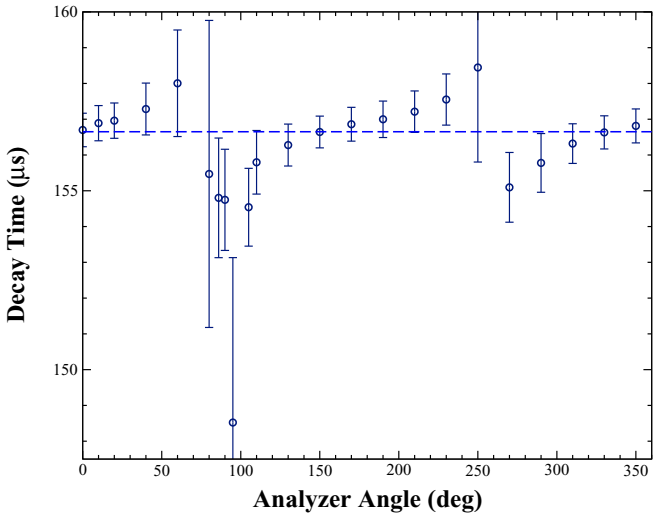

(a)

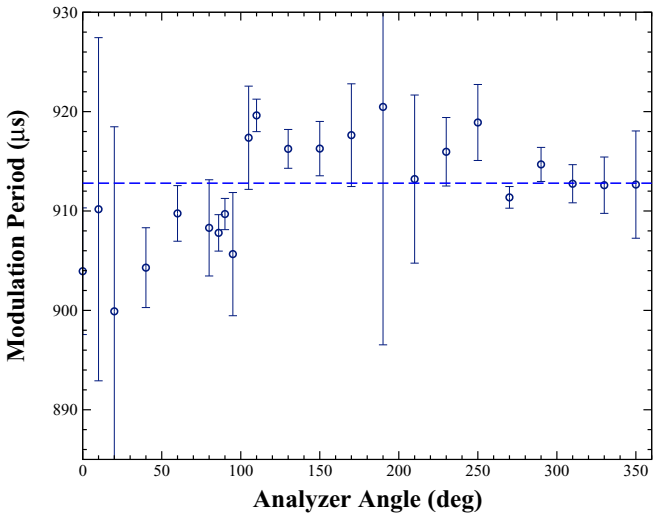

(b)

FIG. 7. (Color online) Analysis of the ring-down time and of the modulation period. (a) Ring-down times, the weighted average value [156.7 (6) μs] is shown, the error bars are reported (50 times the STD provided by the fit process [$\chi^2_{\text{red}} \sim 1.3$]). (b) Modulation period, the weighted average value [912.8 (3.8) μs] is shown, the error bars are reported (100 times the STD provided by the fit process [$\chi^2_{\text{red}} \sim 0.5$]).

acquired during a different day, after reoptimization of the high-finesse cavity. The results can be compared by inspecting Table I.

C. Behavior of the "low-finesse" cavity

A similar set of data has been acquired at 879 nm. It demonstrates a cavity finesse much lower than that previously analyzed. The measurement of the RD times (τ_0) without the insertion of the polarization analyzer indicates that the cavity finesse has moved on from $\mathcal{F} \sim 420\,000$ to $\mathcal{F} \sim 50\,300$. The crude decays are plotted in Fig. 8. This figure clearly shows that the frequency beating almost disappears. This can be explained by observation duration (8 to 9 times τ_0) too short compared with the frequency beating period (assuming that the mirror birefringence remains similar to the value reported

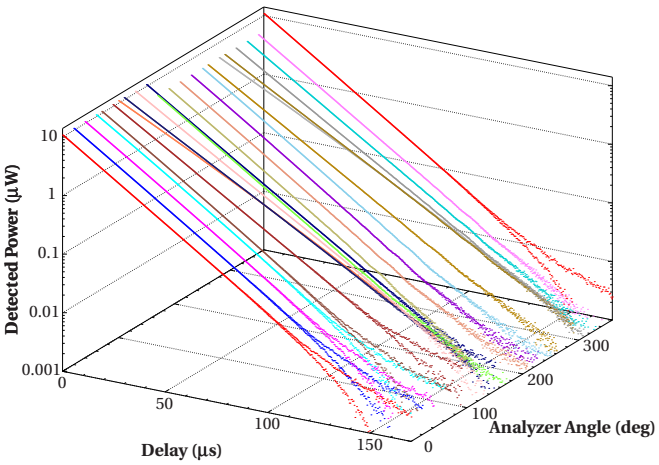

FIG. 8. (Color online) Ring-down decays at 879 nm versus the analyzer angle.

at 796 nm). Nevertheless, variations of the characteristic time can be observed.

Accepting this behavior, we only considered fitting the data by a pure exponential decay (see Fig. 9). Indeed, the distortion of the RD decay time can be recognized as a forerunner indication of the beating: any tentative to observe a period of modulation of $\sim$900 μs over a signal with a characteristics time of only 18 μs is pledged to fail. The large error bars imprinting τ around $\alpha = \pi$ and $3\pi/2$ are correlated with the largest values of the χ^2 coefficient (fit least-squares sum) due to the bare suitability of the exponential decay assumed to match the comparatively low frequency beating hypothesis. Nonetheless, the observed behavior can be modeled by the

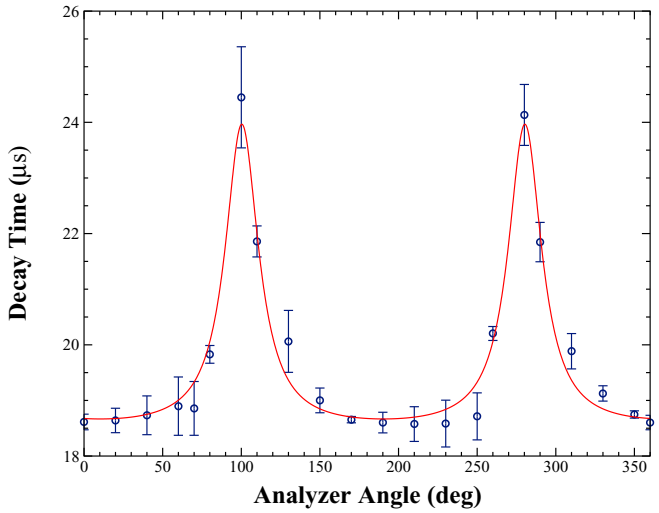

FIG. 9. (Color online) Ring-down time distortion at 879 nm. The RD times have been first obtained by fitting the decays by a pure exponential shape (i.e., without modulation), and then fitted by formula (40). It provides $\tau_e = 18.39\,(6)\,\mu$s, $\tau_m = 5.57\,(44)\,\mu$s, $F'' = 19.4\,(3.6)$, and $\alpha_{\text{off}} = 0.18\,(1)$ rad. The error bars are reported from the fit process of the decays (100 times the STD providing $\chi^2_{\text{red}} \sim 1$).

following *ad hoc* function

$$\tau(\alpha) = \tau_e + \frac{\tau_m}{1 + F'' \cos^2(\alpha - \alpha_{\text{off}})}. \quad (40)$$

The weighted RD times have been fitted by Eq. (40). Two relevant parameters can be discussed: $\tau_e = 18.39\,(6)\,\mu$s, which is very close to the value obtained without analyzer [$18.64\,(9)\,\mu$s], and the polarization analyzer offset $\alpha_{\text{off}} = 10.3\,(7)^\circ$, a value close to those obtained for the high-finesse cavity (see Table I).

We also paid special attention to the acquisition duration since the measurements, obtained close to crossed polarization configurations, required longer acquisition duration (almost two orders of magnitude compared with the *s*-polarization configuration) because of the strong rejection of the polarizer as previously discussed (see Sec. IV B).

V. DISCUSSION

A. Regarding the current study

In the experiences reported here, where the *s* polarization is used to impinge on a high-finesse cavity, the temporal shape of the RD decays clearly exhibits the overall response of a birefringent cavity. This effect has become even more pronounced when a detection close to the *p* polarization was arranged. This is clearly caught for a high-finesse cavity ($\mathcal{F} \sim 420\,000$): a beating frequency close to 1 kHz is observable with an absolute value of the modulation index which can approach 1. A forerunner effect is also observable with a lower finesse cavity ($\mathcal{F} \sim 50\,300$) when addressing the distortions of the RD time (see Table I). Actually, the observation of the frequency beating is demanding for a CW-CRDS setup because there are two conditions to satisfy: the period of the beating should be less than the observation duration, let us say

$$T_{\text{mod}} \leqslant 8\,\tau_0, \quad (41)$$

and the frequency difference between the two eigenpolarization cavity modes should be less than the cavity bandwidth:

$$\omega_{\text{mod}} \lesssim 2\Delta_\omega. \quad (42)$$

Both relations can be summarized by the double inequality

$$\frac{\pi^2}{2\mathcal{F}} \leqslant \epsilon \lesssim \frac{2\pi}{\mathcal{F}}. \quad (43)$$

Actually, relation (43) strongly limits the range of ϵ allowing the frequency beating observation. However, inequality (42) can be relaxed if the two eigenpolarization modes can be simultaneously excited. Accordingly, the present CRDS mode tracking may have some advantages of comparing with a tight PDH locking [57].

The effective cavity birefringence is assumed resulting from the birefringence of the dielectric coating of the individual high reflectors. We cannot distinguish these individual contributions because the relative orientation of the mirrors has not been monitored. Actually, the effective birefringence can vary from day to day if the cavity is reoptimized, for example: the mirrors are sandwiched between an o-ring and a compression ring plate. In addition, the substrates are stressed by the atmospheric pressure while the high-reflection layers are under vacuum.

The birefringence values given in Table I are larger (one order of magnitude) than the values reported previously for individual mirrors under similar conditions but obtained with different techniques [17,38]. Our values suffer from uncertainties which could be reduced by accurately measuring the FSR of the cavity.

As shown in Fig. 7(b), the beating period undergoes "erratic" fluctuations. The error bars fluctuate also: there are certainly larger when the modulation is weak, and when a detection is performed around the *p*-polarization configuration. This is observable in both sets of data obtained for the high-finesse cavity. The averaged values are reported in Table I. The legitimate question is, can these variations ($\pm 11\%$) be correlated with other quantities, or, are they just random ? The comparison of both set of data seems to indicate an absence of trivial correlations. However, a hidden parameter may have been disregarded for sake of ignorance (*vide infra*).

Following the same approach, the RD times are shown in Fig. 7(a) (high-finesse cavity) and in Fig. 8 ("low-finesse" cavity). For the high-finesse cavity, since the beat amplitude has been incorporated in the fit of the RD decays, only marginal variations of τ are expected. Is it right ? Again, it is difficult to assess this hypothesis even if the two weighted mean values of τ (see Table I) are very close, because the fluctuations ($\pm 1\%$, if the data sample at 105° is disregarded) seem to be larger than the error bars. Actually, and unsurprisingly, the error bars are higher around a *p*-polarization detection. The assumption of values of τ independent of α is a key point of the current analysis because the beating are fully considered. This contrasts with the analysis of the lower finesse cavity where only changes of τ can be recognized instead of full beating. Nevertheless, if the *ad hoc* analysis proposed here is relevant, it allows determining $\tau_{\text{min}} \simeq \tau_0$, $\tau_{\text{max}} = \tau_0 + \tau_m$, as well a "peaked" change of τ around the crossed polarization detections, i.e., an amplitude variation $\tau_m \sim 5.5\,\mu$s, in comparison with $\tau_e \sim 18.4\,\mu s$. This behavior can be compared to that observed by Lee and co-worker [70], and by Huang and Lehmann [38]. Both groups observed variations of τ much smoother than those observed here. Nevertheless, applying formula (5) of Ref. [70] to our data would provide a linear birefringence of $7.4\,(7) \times 10^{-6}$ rad, which is a lot less than what we think is the correct cavity birefringence deduced from the frequency beating between the two polarization modes.

Among the possible biases about the "erratic" behavior of τ_0, we must emphasize again the fact that the intracavity power is a function of the analyzer angle (see Fig. 6). The lowest initial intracavity power is estimated at 2.5 W (*s*-polarization detection), while it certainly approaches 200 W in *p*-polarization detection [indeed, this ratio (see Fig. 6) is in good agreement with the values extracted from the acquisition times t_{aq}]. Could local heating, due to the intracavity power, change the mirror birefringence or the mirror reflectance? This should be checked by running the experiment at constant intracavity power. Nonetheless, similar photorefractive power dependent effects have been previously reported [25].

We have also determined the rotation angle (θ) associated with the birefringence [see Eq. (2)]. The two sets of experimental data provide close values (i.e., within the error bars). If the value of θ was null, the observation of the beating would

TABLE I. Data summary. Free-spectral range of the cavity: $f_{FSR} = 429\,(3)$ MHz. τ_0 is the RD time fitted without analyzer. $\langle\tau\rangle$ is the weighted averaged RD time deduced from the fit of formula (39) over all the analyzer angles. τ_e is the RD time deduced from formula (40). Standard errors have been deduced from values provided by both fit packages used (except when specified).

Mirror sets	$\tau_0(\mu s)$	$\langle\tau\rangle(\mu s)$	$\tau_e(\mu s)$	α_{off}(deg)	$\langle T_{mod}\rangle$ (μs)	ϵ (rad)	θ (rad)
Set 1[a] at 796 nm $\Delta_\omega \sim 0.51$ kHz $\mathcal{F} \sim 420\,000$	156.65 (17)	156.7 (6)	na	6.7 (1.6)	912.8 (3.8)	$1.605\,(18) \times 10^{-5}$	$-0.16\,(2)$
Set 2[a] at 796 nm $\Delta_\omega \sim 0.51$ kHz $\mathcal{F} \sim 420\,000$	156.60 (15)	156.6 (3)	na	1.7 (4)	896.5 (3.9)	$1.634\,(15) \times 10^{-5}$	$-0.117\,(2)$
Set 1 at 879 nm $\Delta_\omega \sim 4.3$ kHz $\mathcal{F} \sim 50\,300$	18.64 (9)	na	18.39 (6)	10.3 (7)	na	na	na

[a]See Fig. 5(a).
[b]See Fig. 5(b).

be almost impossible because the modulation would rise only at $\pi/2$ and $3\pi/2$ (ignoring any offset issue on α), i.e., when detecting in p-polarization configuration, while the detected signal is approaching zero. Actually, these two angles are singular. The non-null value of θ allows polarization mixing and detectable frequency beating for almost all the values of the analyzer angle.

The values of θ and of α are two quantities demanding for consideration when optimal amplitude of the beating is concerned: a 100% modulation is actually not reachable experimentally (it is not necessary an instrumental imperfection as suggested by Müller *et al.* [27]). Accordingly, both quantities θ and α control the accuracy of the beating frequency determination. A residual weak ellipticity of the impinging EMF would give rise to a similar behavior.

Under the low-finesse conditions, the behavior of the fluctuations of the RD time seems quite similar to that observed for the high-finesse cavity. Hence, the intracavity power variations can also be evoked since, if the initial power (i.e., before the decay) is less than that of the high-finesse cavity (same triggering voltage threshold), the intracavity power variations versus the analyzer angle are comparable.

Our experimental conditions did not allow us to open a relevant discussion about the dephasing (or delay), shifting the frequency beats [i.e., the parameter ϕ in Eq. (39)], this potential dephasing may contain additional information about the phase to the coupled cavity modes. It should be considered in a future study.

It is worth noting that the individual mirror birefringence cannot be smaller than the effective cavity birefringence [17]. Hence, the relatively large value of the mirror birefringence, when considering the low value of $1 - \mathcal{R}$ (25 ppm), is relatively unexpected (i.e., high) according to the birefringence extrapolations based on the modeling of multilayer stacks [7].

B. Comparison with the data analysis proposed by Berceau *et al.*

It is worthy of attention that the discussion of the results reported here, i.e., the frequency beating resulting from the mirror birefringence lifting the cavity mode degeneracy, does not match the data reported by Berceau *et al.* relative to the temporal response of a high-finesse cavity, built up for BMV experiences [22,23]. In this latter work, the beam issued from the polarized laser source (at 1.064 μm) is first tightly locked (PDH [57]) against the high-finesse cavity ($\mathcal{F} \sim 481\,000$). Then, the beam locking is abruptly interrupted by an AOM to measure the intensity of the leaking intracavity EMF (RD decay). Two detectors allow the simultaneous acquisition of the two orthogonally polarized beams. According to the authors, the intensity of the extraordinary beam can be set at a maximum of extinction (cross-polarizer detection) to allow measuring the total ellipticity. It is the sum of the ellipticity acquired by the beam passing through the cavity, and of the residual ellipticity due to the finite extinction ratio of the polarizer (4×10^{-7}). The exponential behavior of the temporal decay ($\tau_0 \sim 1.16$ ms) is reported thanks to the ordinary beam; it provides the cavity finesse. This datum matches the frequency analysis of the cavity bandwidth at resonance (137 Hz). On the other hand, the temporal shape of the extraordinary beam does not exhibit a pure exponential decay, but shape which could be assimilated to an aperiodic oscillation. The authors analyzed this shape by considering a quadratic time increase of the ellipticity controlled by the cavity characteristic time. Actually, the initial amplitude of the decay is provided by the beam extinction ratio while the time behavior provides what is called the cavity ellipticity, which actually takes a negative value (see formula (13) of Ref. [23]).

Berceau and co-authors approach introduces the concept of effective cavity ellipticity resulting from the accumulation of the mirror ellipticity acquired during the multiple intracavity round trips (previously suggested in Ref. [71]). Actually, when the beam locking is switched off, this effective ellipticity keeps increasing from an initial value, and the polarization is transferred from the ordinary beam to the cross-polarized extraordinary beam. This approach strongly differs from our approach where we consider the intracavity EMF interference: the ellipticity is not accumulated but the mirror birefringence lifts the eigencavity mode (indistinguishable) degeneracy.

C. Outcome

It seems difficult to reconcile the current approach to that proposed by the Toulouse group [22,23]. We think that the frequency beating between two orthogonal eigencavity modes

is clearly established by our data analysis, as well the rotated dephasor contribution (θ). It is based on a solid formalism, and it is in agreement with intracavity induced birefringence (polarimetry) in gases [26,27,35]. Concerning the Toulouse setup, one could suggest (i) to consider the time behavior versus the orientation of the impinging polarization and (ii) to analyze the frequency response (transfer function) of the extraordinary beam, when the laser is locked, since time and frequency behaviors are linked by the Fourier transform in a linear regime (principle of superposition). These are crucial data for the Toulouse cavity since magnetic linear birefringence measurements are targeted.

To help to identify the two different time behaviors, we can emphasize the specific points relative to each setup: (i) the different impinging beam switching modes (straight turning off, versus frequency shifting off resonance), (ii) the frequency mode matching before switching off (loose tracking versus a tight locking), (iii) the intensities of the intracavity power (at least one order of magnitude), (iv) the value of the reported effective mirror birefringence (in a ratio of two orders of magnitude), and (v) the cavity characteristic times ($\sim$157 μs compared with $\sim$1.16 ms). Actually, long ring-down times could unveil an evolution of the mirror birefringence, for example the birefringence sensitivity to the photorefractive effect during the decay.

It is also worth noting that a strict cross-polarization detection is almost impossible with our current experimental setup because of the weakness of the collected signal.

VI. CONCLUSION

To the best of our knowledge, we have shown for the first time that we can observe the frequency beating between the two orthogonal eigenpolarization modes of a linear cavity exhibiting a high-finesse ($\mathcal{F} > 400\,000$ at $\sim$800 nm). This beating results from the residual mirror birefringence. Unfortunately this crude type of CW-CRDS experiment, where the individual cavity mirrors are kept unrotated, does not allow determining the individual birefringence of each mirror which would be actually the most relevant quantity. On the other hand, when the cavity finesse is reduced (here by a factor $\sim$8, i.e., obtained by moving the wavelength to $\sim$880 nm), the beatings are not observable anymore: only alterations of the cavity characteristics (or ring-down) time can be reported. This later behavior has been reported previously and similarly several times, the variations of τ versus the rotation of one of the mirrors had been analyzed to provide the individual mirror birefringence: a specific value of τ ($\tau_{\min}$ and $\tau_{\max}$) being associated with each eigenpolarization.

Here, for the high-finesse configuration, a unique value of the RD time is observed, while the beating frequency remains almost unchanged when the analyzer is rotated ($\epsilon \sim 1.6 \times 10^{-5}$ rad, $\epsilon\,\mathcal{F} \sim 0.65$). We benefit certainly of a loose cavity mode tracking allowing easy probing of the two orthogonal cavity modes. When low birefringence and high-finesse cavity are considered, only dual frequency locking (one against each polarization) may most likely allow measuring of the cavity eigenpolarization frequency shift [25].

We think that this simple CW-CRDS technique may have potential applications when high accurate determination of the birefringence (e.g., of gases) is required. However, this will require fine control of the experimental parameters to reduce the standard deviations and fluctuations observed on the quantities of interest. The differential heating or photorefractive effects, resulting from the variation of the intensity of the EMF trapped inside the cavity versus the detected state of polarization, have been hypothesized.

The full analysis has been possible after carefully examining and modeling the frequency and temporal (obtained by Fourier transformation) behaviors of a high-finesse cavity setup devoted to the CRDS detection. The modeling by Jones matrices has been employed to perform the full calculation.

The presently reported frequency beatings can be favorably compared to those obtained by using pulsed sources (CRDS), for example when analyzing the chirality of molecular gas (i.e., by pulsed CRDS polarimetry or/and ellipsometry). Actually, the finesse of the cavities equipped for polarimetry is strongly reduced, while the induced birefringence (when the cavity is evacuated) is high by construction. Indeed, only changes of the total birefringence (change of the beating frequency) are of interest to analyze the anisotropy effects.

Finally, we also report about disagreements between our data and a recent work obtained with a very high-finesse cavity probed between crossed polarizers.

ACKNOWLEDGMENTS

The data have been obtained at the Grenoble High Magnetic Field Laboratory (MPI-FKF/CNRS). P.D. wishes to thank G. Rikken for the loan of the polarization analyzer. The LPCA is french“laboratoire conventionné au CNRS.”

[1] A. Le Floch and R. Le Naour, Theoretical existence and experimental evidence of basculating eigenvectors in a Fabry-Perot, C. R. Acad. Sci. Ser. B **288**, 225 (1979).

[2] M.-A. Bouchiat and C. Bouchiat, Parity violation in atoms, Rep. Prog. Phys. **60**, 1351 (1997).

[3] L. D. Barron, True and false chirality and parity violation, Chem. Phys. Lett. **123**, 423 (1986).

[4] A. Cotton and H. Mouton, Sur le phénomène de Majorama, C. R. Hebd. Seances Acad. Sci. **141**, 317 (1905).

[5] G. Raffelt and L. Stodolsky, Mixing of the photon with low-mass particles, Phys. Rev. D **37**, 1237 (1988).

[6] M. A. Bouchiat and L. Pottier, Light-polarization modifications in a multipass cavity theoretical and experimental analysis, Appl. Phys. B **29**, 43 (1982).

[7] F. Bielsa, A. Dupays, M. Fouché, R. Battesti, C. Robilliard, and C. Rizzo, Birefringence of interferential mirrors at normal incidence, experimental and computational study, Appl. Phys. B **97**, 457 (2009).

[8] S. Askenazy, J. Billette, P. Dupré, P. Ganau, J-M. Mackowski, J. Marquez, L. Pinard, O. Portugall, D. Ricard, G. L. J. A. Rikken, C. Rizzo, G. Trénec, and J. Vigué, A 25 T dipole pulsed magnet to study the magnetic birefringence of vacuum: The

BMV project, in *Quantum Electrodynamics and Physics of the Vacuum: QED 2000, Second Workshop*, edited by G. Cantatore (AIP, New York, 2001), Vol. 564, p. 115.

[9] R. Battesti, B. Pinto Da Souza, S. Batut, C. Robilliard, G. Bailly, C. Michel, M. Nardone, L. Pinard, O. Portugall, G. Trénec, J.-M. Mackowski, G. L. J. A. Rikken, J. Vigué, and C. Rizzo, The BMV experiment: A novel apparatus to study the propagation of light in a transverse magnetic field, Eur. Phys. J. D **46**, 323 (2008).

[10] J. Alnis, A. Matveev, N. Kolachevsky, Th. Udem, and T. W. Hänsch, Subhertz linewidth diode lasers by stabilization to vibrationally and thermally compensated ultralow-expansion glass Fabry-Pérot cavities, Phys. Rev. A **77**, 053809 (2008).

[11] K. K. Lehmann and D. Romanini, The superposition principle and cavity ring-down spectroscopy, J. Chem. Phys. **105**, 10263 (1996).

[12] P. Dupré, Sub-Doppler noise-immune cavity-enhanced optical heterodyne molecular spectrometry modeling: From Doppler broadening to cross-sideband resonances, J. Opt. Soc. Am. B **32**, 838 (2015).

[13] P. Dupré, Saturated absorption and crossover resonances in a high-finesse cavity: Formalism and application to the hyperfine structure of jet-cooled NO_2 by saturated-absorption cavity-ring-down spectroscopy, Phys. Rev. A **85**, 042503 (2012).

[14] S. Carusotto, E. Polacco, E. Iacopini, G. Stefanini, E. Zavattini, and F. Scuri, The ellipticity introduced by interferential mirrors on a linearly polarized light beam orthogonally reflected, Appl. Phys. B **48**, 231 (1989).

[15] D. Jacob, M. Vallet, F. Bretenaker, A. Le-Floch, and M. Oger, Supermirror phase anisotropy measurement, Opt. Lett. **20**, 671 (1995).

[16] S. Moriwaki, H. Sakaida, T. Yuzawa, and N. Mio, Measurement of the residual birefringence of interferential mirrors using Fabry-Perot cavity, Appl. Phys. B **65**, 347 (1997).

[17] F. Brandi, F. Della Valle, A. M. De Riva, P. Micossi, F. Perrone, C. Rizzo, G. Ruoso, and G. Zavattini, Measurement of the phase anisotropy of very high reflectivity interferential mirrors, Appl. Phys. B **65**, 351 (1997).

[18] M. Vallet, F. Bretenaker, A. Le Floch, R. Le Naour, and M. Oger, The Malus Fabry-Perot interferometer, Opt. Commun. **168**, 423 (1999).

[19] E. Inbar and A. Arie, High-sensitivity measurements of the kerr constant in gases using a Fabry-Perot-based ellipsometer, Appl. Phys. B **70**, 849 (2000).

[20] J. Morville and D. Romanini, Sensitive birefringence measurement in a high-finesse resonator using diode laser optical self-locking, Appl. Phys. B **74**, 495 (2002).

[21] M. Durand, J. Morville, and D. Romanini, Shot-noise-limited measurement of sub–parts-per-trillion birefringence phase shift in a high-finesse cavity, Phys. Rev. A **82**, 031803 (2010).

[22] P. Berceau, M. Fouché, R. Battesti, F. Bielsa, J. Mauchain, and C. Rizzo, Dynamical behaviour of birefringent Fabry–Perot cavities, Appl. Phys. B **100**, 803 (2010).

[23] P. Berceau, M. Fouché, R. Battesti, and C. Rizzo, Magnetic linear birefringence measurements using pulsed fields, Phys. Rev. A **85**, 013837 (2012).

[24] A. Le Floch, R. Le Naour, G. Stephan, and P. Brun, Frequency stabilization and tunability of lasers; use of mobile dips and peaks, Appl. Opt. **15**, 2673 (1976).

[25] J. L. Hall, J. Ye, and L.-S. Ma, Measurement of mirror birefringence at the sub-ppm level: Proposed application to a test of QED, Phys. Rev. A **62**, 013815 (2000).

[26] T. Müller, K. B. Wiberg, and P. H. Vaccaro, Cavity ring-down polarimetry (CRDP): A new scheme for probing circular birefringence and circular dichroism in the gas phase, J. Phys. Chem. A **104**, 5959 (2000).

[27] T. Müller, K. B. Wiberg, P. H. Vaccaro, J. R. Cheeseman, and M. J. Frisch, Cavity ring-down polarimetry (CRDP): Theoretical and experimental characterization, J. Opt. Soc. Am. B **19**, 125 (2002).

[28] S. M. Wilson, K. B. Wiberg, J. R. Cheeseman, M. J. Frisch, and P. H. Vaccaro, Nonresonant optical activity of isolated organic molecules, J. Phys. Chem. A **109**, 11752 (2005).

[29] M. A. Everest, V. M. Papadakis, K. Stamataki, S. Tzortzakis, B. Loppinet, and T. P. Rakitzis, Evanescent-wave cavity ring-down ellipsometry, J. Phys. Chem. Lett. **2**, 1324 (2011).

[30] K. Stamataki, V. Papadakis, M. A. Everest, S. Tzortzakis, B. Loppinet, and T. P. Rakitzis, Monitoring adsorption and sedimentation using evanescent-wave cavity ringdown ellipsometry, Appl. Opt. **52**, 1086 (2013).

[31] D. Sofikitis, K. Stamataki, A. K. Spiliotis, M. A. Everest, S. Papadakis, J.-L. Stehle, B. Loppinet, and T. P. Rakitzis, Sensitivity enhancement for evanescent-wave sensing using cavity-ring-down ellipsometry, Opt. Lett. **38**, 1224 (2013).

[32] D. Sofikitis, L. Bougas, G. E. Katsoprinakis, A. K. Spiliotis, B. Loppinet, and T. P. Rakitzis, Evanescent-wave and ambient chiral sensing by signal-reversing cavity ringdown polarimetry, Nature (London) **514**, 76 (2014).

[33] D. Sofikitis, A. K. Spiliotis, K. Stamataki, G. E. Katsoprinakis, L. Bougas, P. C. Samartzis, B. Loppinet, T. P. Rakitzis, M. Surligas, and S. Papadakis, Microsecond-resolved SDR-based cavity ring down ellipsometry, Appl. Opt. **54**, 5861 (2015).

[34] A. Karaiskou, V. Papadakis, B. Loppinet, and T. Peter Rakitzis, Cavity ring-down ellipsometry, J. Chem. Phys. **131**, 121101 (2009).

[35] L. Bougas, G. E. Katsoprinakis, W. von Klitzing, J. Sapirstein, and T. P. Rakitzis, Cavity-Enhanced Parity-Nonconserving Optical Rotation in Metastable Xe and Hg, Phys. Rev. Lett. **108**, 210801 (2012).

[36] L. Bougas, G. E. Katsoprinakis, W. von Klitzing, and T. P. Rakitzis, Fundamentals of cavity-enhanced polarimetry for parity-nonconserving optical rotation measurements: Application to Xe, Hg, and I, Phys. Rev. A **89**, 052127 (2014).

[37] R. Engeln, G. Berden, E. van den Berg, and G. Meijer, Polarization dependent cavity ring down spectroscopy, J. Chem. Phys. **107**, 4458 (1997).

[38] H. Huang and K. K. Lehmann, Effects of linear birefringence and polarization-dependent loss of supermirrors in cavity ring-down spectroscopy, Appl. Opt. **47**, 3817 (2008).

[39] K. W. Busch and M. A. Busch, editors, Cavity Ringdown Spectroscopy: An Ultratrace-Absorption Measurement Technique, Vol. 720 of *ACS Symposium Series* (Oxford University Press, Oxford, 1999).

[40] J. J. Scherer, P. B. Paul, A. O'Keefe, and R. J. Saykally, Cavity ringdown laser absorption spectroscopy: History, development and application to pulsed molecular beams, Chem. Rev. **97**, 25 (1997).

[41] M. D. Wheeler, S. M. Newman, A. J. Orr-Ewing, and M. N. R. Ashold, Cavity ring-down spectroscopy, J. Chem. Soc. Faraday Trans. **94**, 337 (1998).

[42] S. Cheskis, Quantitative measurements of absolute concentrations of intermediate species in flames, Progress Energy Combust. Sci. **25**, 233 (1999).

[43] A. O'Keefe, J. J. Scherer, J. B. Paul, and R. J. Saykally, Cavity-ringdown laser spectroscopy history, development, and applications, in *Cavity Ringdown Spectroscopy: An Ultratrace-Absorption Measurement Technique*, edited by K. W. Busch and M. A. Busch, Vol. 720 of ACS Symposium Series, (Oxford University Press, Washington, DC, 1999), p. 71.

[44] G. Berden, R. Peeters, and G. Meijer, Cavity ring down spectroscopy: Experimental schemes and applications, Int. Rev. Phys. Chem. **19**, 565 (2000).

[45] R. Peeters, G. Berden, and G. Meijer, Sensitive absorption techniques for spectroscopy, Am. Lab. **33**, 60 (2001).

[46] D. B. Atkinson, Solving chemical problems of environmental importance using cavity ring-down spectroscopy, Analyst **128**, 117 (2003).

[47] P. Dupré, Probing molecular species by cavity ringdown laser absorption spectroscopy, application to the spectroscopy and dynamics of jet-cooled NO_2, C. R. Acad. Sci. Paris, Ser. IV **2**, 929 (2001).

[48] A. Kastler, Transmission d'une impulsion lumineuse par un interféromètre Perot-Fabry, Nouv. Rev. Opt. **5**, 133 (1974).

[49] D. Z. Anderson, J. C. Frisch, and C. S. Masser, Mirror reflectometer based on optical decay time, Appl. Opt. **23**, 1238 (1984).

[50] J. Y. Lee, H-W. Lee, and J. W. Hahn, Time domain study on cavity ring-down signals from a Fabry-Pérot cavity under pulsed laser excitations, Jpn. J. Appl. Phys. **38**, 6287 (1999).

[51] H. Naus, I. H. M. van Stokkum, W. Hogervorst, and W. Ubachs, Quantitative analysis of decay transients applied to a multimode pulsed cavity ringdown experiment, Appl. Opt. **40**, 4416 (2001).

[52] Y. He, M. Hippler, and M. Quack, High-resolution cavity ring-down absorption spectroscopy of nitrous oxide and chloroform using a near-infrared cw diode laser, Chem. Phys. Lett. **289**, 527 (1998).

[53] A. M. Shaw, R. N. Zare, C. V. Bennett, and B. H. Kolner, Bounce-by-bounce cavity ring-down spectroscopy: Femtosecond temporal imaging, Chem. Phys. Chem. **2**, 118 (2001).

[54] D. Romanini, P. Dupré, and R. Jost, Non-linear effects by continuous wave cavity ringdown spectroscopy in jet-cooled NO_2, Vib. Spectrosc. **19**, 93 (1999).

[55] G. Giusfredi, S. Bartalini, S. Borri, P. Cancio, I. Galli, D. Mazzotti, and P. De Natale, Saturated-Absorption Cavity Ring-Down Spectroscopy, Phys. Rev. Lett. **104**, 110801 (2010).

[56] J. Cachenaut, C. Man, P. Cerez, A. Brillet, F. Stoeckel, A. Jourdan, and F. Hartmann, Description and accuracy tests of an improved lambdameter, Rev. Phys. Appl. **14**, 685 (1979).

[57] R. W. P. Drever, J. L. Hall, F. V. Kowalski, J. Hough, G. M. Ford, A. J. Munley, and H. Ward, Laser phase and frequency stabilization using an optical resonator, Appl. Phys. B **31**, 97 (1983).

[58] R. G. DeVoe and R. G. Brewer, Laser-frequency division and stabilization, Phys. Rev. A **30**, 2827 (1984).

[59] R. W. Boyd, *Nonlinear Optics*, 3rd ed. (Academic Press, Amsterdam, 2008).

[60] D. W. Kammler, *A First Course in Fourier Analysis* (Prentice Hall, Englewood Cliffs, NJ, 2000).

[61] R. C. Jones, A new calculus for the treatment of optical systems. I. Description and discussion of the calculus, J. Opt. Soc. Am. **31**, 488 (1941).

[62] Rasheed M. A. Azzam and N. M. Bashara, *Ellipsometry and Polarized Light* (North-Holland, Amsterdam, 1987).

[63] D. Hils and J. L. Hall, Response of a Fabry-Perot cavity to phase modulated light, Rev. Sci. Instrum. **58**, 1406 (1987).

[64] N. Uehara and K. Ueda, Accurate measurement of ultralow loss in a high-finesse Fabry-Perot interferometer using the frequency response functions, Appl. Phys. B **61**, 9 (1995).

[65] A. Kastler, Atoms à l'intérieur d'un interféromètre Perot-Fabry, Appl. Opt. **1**, 17 (1962).

[66] Gnuplot: A portable, multiplatform, command-line driven graphing utility, http://sourceforge.net/projects/gnuplot.

[67] F. James and M. Roos, Minuit - A system for function minimization and analysis of the parameter errors and correlations, Comp. Phys. Commun. **10**, 343 (1975).

[68] M. Hatlo, F. James, P. Mato, L. Moneta, M. Winkler, and A. Zsenei, Developments of mathematical software libraries for the LHC experiments, IEEE Trans. Nucl. Sci. **52**, 2818 (2005).

[69] P. R. Bevington and D. K. Robinson, *Data Reduction and Error Analysis for the Physical Sciences*, 2nd ed. (McGraw-Hill, New York, 1992).

[70] J. Y. Lee, H-W. Lee, J. W. Kim, Y. S. Yoo, and J. W. Hahn, Measurement of ultralow supermirror birefringence by use of the polarimetric differential cavity ringdown technique, Appl. Opt. **39**, 1941 (2000).

[71] J. Poirson, M. Vallet, F. Bretenaker, A. Le Floch, and J-Y. Thépot, Resonant cavity gas-phase polarimeter, Anal. Chem. **70**, 4636 (1998).